



Microstructural and mechanical anisotropy in pressure-assisted sintered copper nanoparticles

Downloaded from: <https://research.chalmers.se>, 2025-02-22 21:27 UTC

Citation for the original published paper (version of record):

Du, L., Liu, K., Hu, D. et al (2025). Microstructural and mechanical anisotropy in pressure-assisted sintered copper nanoparticles. *Acta Materialia*, 287. <http://dx.doi.org/10.1016/j.actamat.2025.120772>

N.B. When citing this work, cite the original published paper.



Full length article

Microstructural and mechanical anisotropy in pressure-assisted sintered copper nanoparticles

Leiming Du ^a, Kai Liu ^{b,1}, Dong Hu ^a, Olof Bäcké ^c, Xiao Hu ^a, Xinrui Ji ^a, Jiajie Fan ^d, René H. Poelma ^{e,*}, Magnus Hörnqvist Colliander ^c, Guoqi Zhang ^{a,*}

^a Department of Microelectronics, Delft University of Technology, Mekelweg 4, Delft, 2628 CD, The Netherlands

^b Department of Materials Science and Engineering, Delft University of Technology, Mekelweg 2, Delft, 2628 CD, The Netherlands

^c Department of Physics, Chalmers University of Technology, Kemigården 1, Gothenburg, 412 96, Sweden

^d Shanghai Engineering Technology Research Center for SiC Power Device, Academy for Engineering & Technology, Fudan University, 220 Handan Rd., Shanghai, 200433, China

^e Nexperia, Jonkerbosplein 52, Nijmegen, 6534 AB, The Netherlands

ARTICLE INFO

Keywords:

Sintered Cu nanoparticles
Micro-cantilever bending tests
Anisotropy
3D reconstruction
Molecular dynamics simulation

ABSTRACT

The mechanical strength of sintered nanoparticles (NPs) limits their application in advanced electronics packaging. In this study, we explore the anisotropy in the microstructure and mechanical properties of sintered copper (Cu) NPs by combining experimental techniques with molecular dynamics (MD) simulations. We establish a clear relationship between processing conditions, microstructural evolution, and resulting properties in pressure-assisted sintering of Cu NPs. Our findings reveal that pressure-assisted sintering induces significant anisotropy in the microstructure, as evidenced by variations in areal relative density and the orientation distribution of necks formed during sintering. Specifically, along the direction of applied pressure, the microstructure exhibits reduced variation in areal relative density and a higher prevalence of necks with favorable orientations. The resulting anisotropic mechanical properties, with significantly higher strength along the pressure direction compared to other directions, are demonstrated through micro-cantilever bending tests and tensile simulations. This anisotropy is further explained by the combined effects of strain localization (influenced by areal relative density) and the failure modes of necks (determined by their orientation relative to the loading direction). This work provides valuable insights into the analysis of sintered NPs microstructures and offers guidance for optimizing the sintering process.

1. Introduction

Wide band gap (WBG) materials like silicon carbide (SiC) and gallium nitride (GaN) have been widely used in power modules owing to their excellent electric and thermal properties and performance [1–3], especially when operated at high breakdown voltages and high temperatures (< 200 °C). Traditional interconnect bonding materials like Sn- or Pb-based solder alloys face limitations in power devices due to the low melting point, limited thermal conductivity and insufficient creep resistance [4–7]. In recent years, sintered silver (Ag) and copper (Cu) nanoparticles (NPs) interconnects are proposed as an alternative to solder alloys in the die-attachment of WBG semiconductors because of their low sintering temperature, high melting temperature and high electrical and thermal conductivity [8–12].

Despite these advantages, the anisotropy of the microstructure and mechanical properties of sintered Cu NPs poses a critical challenge

for the bonding quality and long-term reliability of joints. NPs sintering is characterized by low sintering temperatures (less than 300 °C), short sintering times, and the assistance of uniaxial compressive stress [13]. This process, while efficient, inherently induces anisotropy in the sintered microstructure. Many experiments have highlighted the anisotropy in micrometer-sized particles, such as alumina and Cu, when sintered with uniaxial compressive stress [14–16]. The sintered bodies exhibit greater shrinkage in the direction of the applied stress. At the microscale, this anisotropy originates from the evolution and orientation change of the pores [14]. The aspect ratio of the pores increases after sintering, and the orientation of the long axis tends to align parallel to the stress direction [17,18]. Additionally, the constraints imposed by the substrate on particle merging affect the shape of the pores [19]. For Cu NPs, the sintered microstructure is highly porous,

* Corresponding authors.

E-mail addresses: rene.poelma@nexperia.com (R.H. Poelma), magnus.colliander@chalmers.se (M.H. Colliander), G.Q.Zhang@tudelft.nl (G. Zhang).

¹ Equal Contribution.

and the anisotropy is even more pronounced under these conditions. From a bonding quality perspective, this anisotropy can lead to uneven stress distribution within the joint, particularly during thermal cycling or mechanical loading [16], potentially compromising the structural integrity. Furthermore, from a reliability viewpoint, local variations in mechanical properties can influence crack initiation and propagation pathways [20], significantly affecting the long-term performance. These concerns are especially critical for SiC devices, which often operate under extreme conditions, including high temperatures and power densities. Addressing the anisotropy in the microstructure and mechanical properties of sintered Cu NPs is therefore essential. Given the sintering conditions for NPs, the resulting microstructure after sintering is highly porous, and severe anisotropy is expected [15].

The high porosity and small feature sizes of sintered NPs pose challenges for mechanical property testing and microstructure characterization. Scanning electron microscopy (SEM) and transmission electron microscopy (TEM) are widely used for microstructure observation, such as examining pore shapes and necks formed during sintering. Zuo et al. [21] studied the microstructure evolution of Cu NPs during pressureless sintering. The grain growth and grain boundary movement were clearly observed using TEM at elevated temperature. Since the spatial features of particle packing and pore distribution strongly influence the electrical, thermal, and elastic properties of sintered NPs, three-dimensional (3D) characterization of the microstructure is crucial. Two methods for 3D reconstruction have been reported: focused ion beam combined with scanning electron microscopy (FIB-SEM) [22–24], and synchrotron X-ray computed tomography [25,26]. Through 3D reconstruction, the inter-particle necks can be identified, and the evolution of the microstructure can be described using metrics such as pore numbers [23], mean intercept length [24], and particle shape [25]. Areal relative density curves have also been proposed to illustrate variations in local microstructure [22,27].

The mechanical properties of sintered NPs are typically measured with micropillar compression tests [28] and micro-cantilever bending tests [29–31]. Chen et al. [29] studied the effect of micro-cantilever size (20, 10 and 5 μm in width) on fracture toughness of sintered Ag NPs by micro-cantilever bending tests, revealing that fracture toughness decreases as specimen size decreases. Recently, we studied the effect of depth of pre-crack on the fracture toughness of sintered Cu NPs by micro-cantilever bending tests [31]. Results show that microscopic fracture toughness presents a limited relationship with notch depth.

Due to difficulties in experiments, simulation methods spanning multiple length and time scales are applied to investigate various aspects of NPs sintering. Discrete element modeling (DEM) primarily focuses on the particle packing [19] and neck formation during sintering [32]. Specifically, Wonisch et al. [33] analyzed the anisotropic microstructure of sintered micro-sized particles induced by external stress using both experiments and DEM, identifying the size of contact areas in different directions as a crucial factor. The grain growth and evolution of pores during sintering process are also studied using phase field simulation in both two-dimensional (2D) [34] and 3D [35,36] models. The relationship between microstructure and properties is modeled using finite element method (FEM) [37,38] and phase field methods [39]. The porous structure for the simulation are from SEM images [37] and stochastic modeling [38,39].

Molecular dynamics (MD) simulations have been used to study the NPs sintering process and subsequent mechanical tests. Two-particle models are extensively utilized to examine atom diffusion and neck formation during sintering [40–42]. Multi-particle sintering has also been explored with MD [43–45]. Guo et al. simulated the densification process of a high-entropy alloy to show the influence of initial particle packing [44]. The accuracy and effectiveness of the multiple particles sintering model were verified using a phase-field model. This method was also applied to investigate the influence of initial particle morphology on the sintering of gold NPs [45]. Due to the limited timescale of MD simulations, the contributions of diffusion mechanisms, such as

surface diffusion and bulk diffusion, are underestimated, and densification in these simulations is mainly caused by plastic flow under stress. However, MD simulations are expected to yield physically meaningful results considering the short sintering time and low temperature characteristic of NP sintering. Additionally, Zuo et al. [21] demonstrated that without external stress, grain growth and grain boundary mobility are insignificant at 220 $^{\circ}\text{C}$.

This paper aims to elucidate the relationship between sintering methods and microstructural anisotropy, as well as the anisotropy of mechanical properties, through a combination of experiments and simulations. Section 2 details the experimental and simulation methods. In Section 3, the microstructure of sintered Cu NPs from FIB-SEM reconstruction, precession electron diffraction (PED) and MD simulations are analyzed based on areal relative density and neck formation during sintering. The origin of microstructural anisotropy is discussed. In Section 4, the strength of sintered NPs is measured by micro-cantilever bending tests and tensile simulations, and the anisotropic strength of sintered Cu NPs is connected with their microstructure.

2. Experimental and simulation procedure

2.1. Cu NPs and sintered sample preparation

The Cu paste used in this study was prepared by a reductive pretreatment method [46]. Fig. 1(a) presents an SEM image of the Cu NPs, showing them as quasi-spherical and uniformly distributed with an average size (diameter) of 150 nm (Fig. 1(b)). Energy dispersive spectroscopy (EDS) was conducted on the cross-section, confirming the sintered Cu NPs is almost pure with minimal oxidation, as shown in Fig. 1(c). A die-attach structure (Cu dummy die, sintered Cu NPs layer, and Cu substrate) was prepared using pressure-assisted sintering technology. As illustrated in Fig. 1(d), the Cu paste was firstly transferred onto the Cu substrate with a stencil thickness of 100 μm using a screen printer and a flat scraper. Second, the substrate was heated to 120 $^{\circ}\text{C}$ for 5 min to evaporate the organic solvent after removing the stencil. Then, the Cu dummy dies were attached to the substrates using a vacuum pick-up pen. Pressure-assisted sintering was conducted in a nitrogen atmosphere (Applied Microengineering Ltd., UK). The Cu paste was sintered for 10 min at 250 $^{\circ}\text{C}$ under 25 MPa uniaxial stress in a reducing atmosphere (5% H_2/N_2). Finally, the sintered sample (Fig. 1(e)) was removed from the furnace after cooling down. The schematic diagram of the die-attach structure in power electronics is shown in Fig. 1(f).

2.2. FIB-SEM tomography

FIB-SEM tomography, an SEM-based technique, enables advanced characterization and improved understanding of 2D results. Here, we used FIB-SEM tomography to characterize the void distribution in sintered Cu NPs. The methodology involved using a dual-beam FEI Helios G4 CX FIB-SEM system for imaging and slicing to reconstruct 3D structures. Before ion milling, a platinum protective layer, approximately 1 μm thick, was deposited on the region of interest to prevent damage during ion milling. Subsequently, fiducial markers were strategically placed on the samples, allowing for real-time drift correction between successive milling operations. To facilitate FIB-SEM tomography, the sample was tilted at 52 $^{\circ}$, enabling milling perpendicular to the surface. Additionally, a U-shaped trench was milled alongside the area of interest to create space for redepositing material removed during tomography. The FIB slicing was conducted at an accelerating voltage of 30 kV and 40 pA, and SEM images were taken at 10 kV using an SE detector. The Auto Slice and View software (ASV4) was utilized to automate the tomography process by estimating the next slice position based on the top view image.

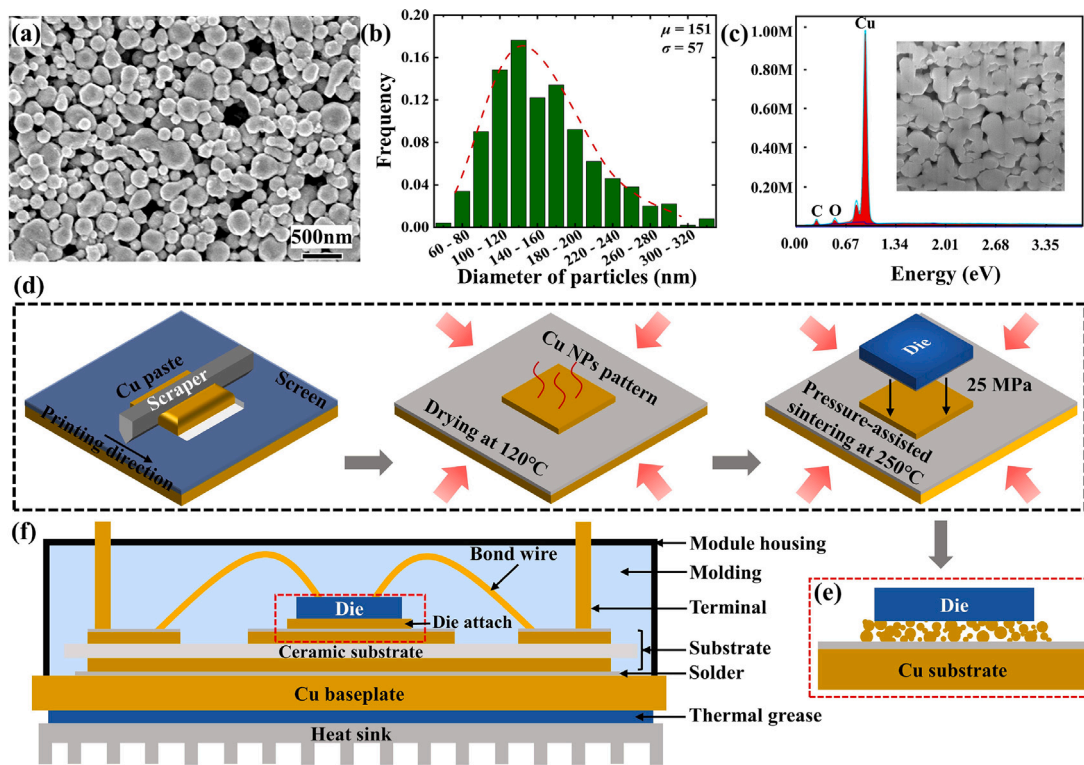


Fig. 1. (a) SEM image of the Cu NPs; (b) size (diameter) distribution; (c) EDS Spectrum of the sintered Cu NPs; (d) pressure-assisted sintering technique; (e) schematic diagram of sintered die-attach structure; (f) schematic diagram of the die-attach structure in power electronics.

2.3. Precession electron diffraction

To characterize the grain orientation of sintered Cu NPs, PED [47–54], a state-of-the-art transmission electron microscopy (TEM)-based technique was employed in this study. PED was performed using a JEM-2200FS (JEOL) TEM operating at 200 kV and equipped with the ASTAR system (Nanomegas) [53]. The microscope was operated in nanobeam diffraction (NBD) mode with the smallest spot size and a condenser aperture of 10 μm . The probe diameter was approximately 1 nm with a convergence angle of 2 mrad. A precession frequency of 100 Hz and a precession angle of 0.5° were applied during nanobeam scanning. This configuration reduces dynamical diffraction effects and enables reliable orientation and phase identification by integrating intensities over multiple diffraction conditions. By tilting the incident electron beam in a conical motion, PED reduces dynamical diffraction effects and enhances the reliability of orientation and phase identification. Compared to conventional techniques such as electron backscatter diffraction (EBSD) with 50–100 nm [49] and transmission Kikuchi diffraction (TKD) with 10–20 nm [54], PED offers superior resolution down to 1 nm, sensitivity to weak reflections, and the ability to analyze thin samples, making it particularly suitable for nanocrystalline materials. These advantages establish PED as a critical tool for detailed microstructural analysis and phase fingerprinting in advanced materials research.

2.4. Micro-cantilever bending tests

Micro-cantilever bending test is an effective technique for probing the mechanical properties of microscale samples [55,56]. As shown in Fig. 2(a), three kinds of micro-cantilevers with different orientations with respect to the direction of external pressure during sintering were fabricated, i.e. 0° (perpendicular), 45°, and 90° (parallel). For each orientation, six specimens were prepared to ensure the reliability of the data. Fig. 2(b) illustrates that the fabrication process involved five

steps: milling a notch with a low ion current (10 pA), creating U-shaped trenches with a large beam current (20 nA), tilting and milling the base with 3 nA, rotating and repeating on the other side, and forming the micro-cantilever by undercutting. The micro-cantilever was then polished with 1 nA to ensure symmetry and cleaned with 100 pA to minimize damage. A precise marking was made on the free end to establish a well-defined loading point. Fig. 2(c) shows a typical SEM image of the micro-cantilever, and the dimensions of all the micro-cantilevers are shown in Table S1. The micro-cantilevers were fabricated at the middle position of the die-attach layer. This choice was deliberate to ensure consistency in the microstructure and minimize variations caused by non-uniformities during sintering [57]. The middle region is more representative of the average sintering degree and microstructure, as the edges may experience different thermal and pressure conditions [58]. By focusing on this central position, the influence of local non-uniformity was reduced [59], leading to more reliable and reproducible mechanical property measurements. The micro-cantilever has a pentagonal cross-section. We chose this shape for two reasons: it provides more flexibility in selecting the location compared to a rectangular shape, and the stress distribution in a pentagonal cross-section is less affected by preparation inaccuracies, leading to more reliable mechanical property measurements [60,61].

An in-situ nanoindenter setup from Alemnis AG (Switzerland) was utilized to perform micro-cantilever bending tests in a Zeiss Ultra55 FEG SEM chamber. Before conducting the bending tests, the SEM carefully positioned the indenter tip to the fiducial mark on the top surface of the micro-cantilever, as shown in Fig. 2(c). The quasi-static bending test is controlled by displacement. A constant load rate of 10 nm s⁻¹ was applied for all micro-cantilevers until fracture occurred. The bending load was applied with a conospherical diamond tip (radius = 1 μm). Compared with the sharp-tipped indenter, such as the Berkovich indenter, the conospherical indenter with a spherical tip exhibited minimal indentation on the surface of the micro-cantilever [62].

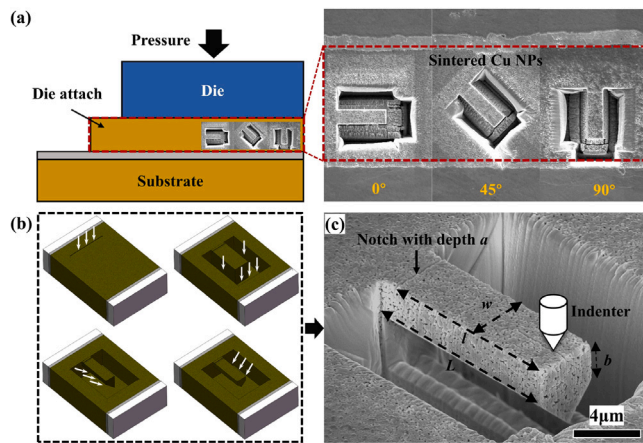


Fig. 2. (a) Relationship of micro-cantilever orientations with pressure during sintering process; (b) FIB process for micro-cantilever fabrication; (c) SEM image of a micro-cantilever.

2.5. MD simulations of the sintering process and tensile tests

The sintering and tensile process were simulated by the MD method using Large-scale Atomic/Molecular Massively Parallel Simulator (LAMMPS) software [63]. The atomic configurations were visualized and analyzed with the Open Visualization Tool (OVITO) [64]. The Cu embedded atom method (EAM) interatomic potential proposed by Mishin et al. [65] is employed to describe the atomic interaction, which has been successfully applied in simulating various mechanical properties and microscopic phenomena in Cu, such as diffusion and grain boundary migration [66–68]. The melting point of bulk Cu within this potential is 1273 ± 30 K, which matches well with the experimentally observed value of 1358 K. The initial Cu particle model has the following characteristics: spherical shape, non-contact or point-contact interactions between particles, a total volume fraction of about 45%, random spatial orientation of each particle, and a particle size distribution that is comparable to experimental observation. To enhance computational efficiency, the particle diameter in the simulation was 3–12 nm, as shown in Fig. 3(b). Similar values (2–15 nm) have been used in previous MD simulations of the sintering process of Cu NPs [41]. Moreover, since Fig. 1(c) shows that the organic substances evaporated during the sintering process, the influence of the organic binder in the sintering process is ignored.

The procedure for generating 3D models of Cu NPs is as follows:

1. Select a point in 3D space randomly to be the center of the Cu NPs. The particle radius is determined by a randomly generated number that follows a normal distribution
2. Validate the new particle by making sure it does not overlap with existing spheres considering the periodic boundary condition (PBC).
3. Assign a random orientation to the particle.
4. Repeat the procedure until the acceptance rate is very low.
5. Select particles randomly and expand them until they meet each other.
6. Execute energy minimization by employing the conjugate gradient (CG) algorithm.

Fig. 3(a) shows the resulting particle model of Cu NPs, which is color-coded with Adaptive Common Neighbor Analysis and has dimensions of roughly $450 \times 450 \times 450 \text{ Å}^3$, consisting of around 240 particles and 3.6 million atoms. The initial relative density of the model is approximately 45%. Two types of external stresses (uniaxial and hydrostatic) during the sintering process are considered in MD simulation. The models sintered under uniaxial and hydrostatic stress are labeled as US and HS, respectively. The sintering method employed in US model is similar to sintering process in Section 2.1, while the HS

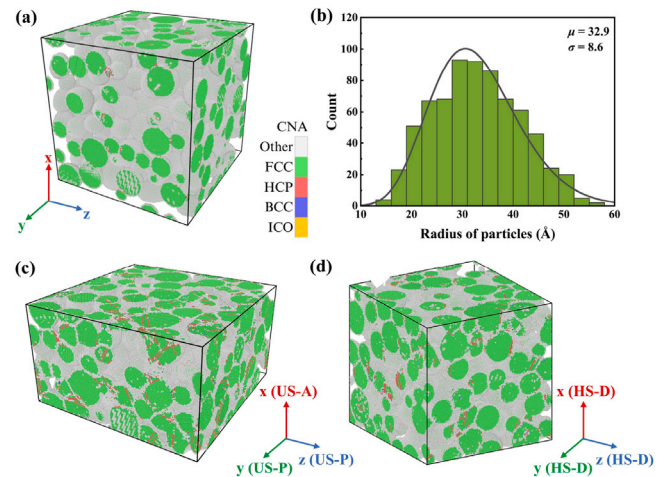


Fig. 3. 3D Cu NPs model (a) before and after (c, d) sintering. (b) radius value distribution of Cu NPs; (c) after uniaxial stress sintering along the X-axis; (d) after hydrostatic stress sintering.

model shares similarities with a constrained sintering method reported in [69].

The sintering process in the MD simulation includes three stages. Initially, the temperature increases to 523 K (in consistent to the experiments) with a Nose–Hoover thermostat at a speed of 2 K/ps. Subsequently, a uniaxial strain is applied to the US model, with strain rate of $1 \times 10^9 \text{ s}^{-1}$. The pressure in the non-compressed direction is maintained at 0, corresponding to the sintering process in experiments which is unconstrained in the non-loading direction. The overall deformation along strain direction is 40%, according to the height changes of the powder during sintering in experiments (roughly from 1.8 μm to 1.3 μm). For the HS model, a hydrostatic stress is applied on all surfaces during the sintering process until the relative density reaches the same level as the US model. The loading rate is 0.2 MPa/ps. The sintering process finishes after approximately 800 ps. Finally, the temperature is kept at 523 K, the volume remains constant, and a relaxation period of 100 ps is applied to eliminate the additional stress caused by the high strain rate in the previous loading step. The US and HS models after sintering are shown in Figs. 3(c) and (d), respectively.

Due to the significant anisotropy of models after sintering on both microstructure and mechanical performance, directional terminology is introduced for convenience of description. The direction aligned with the stress direction during sintering is labeled as US-A, while the direction perpendicular to the stress direction during sintering is denoted as US-P, as shown in Fig. 3(c). Note that US-A and US-P represent the loading and observation directions. However, such distinction is not necessary for HS models, and all three orientations are labeled as HS-D, as shown in Fig. 3(d). Given the impact of the initial particle distribution on sintering and mechanical performance, three independent models with random initial particle packing are employed. Consequently, the models included in this research and their quantities are outlined in Table S2. Before simulating the tensile process, a relaxation procedure with variable box dimensions is implemented to ensure that the model has no residual internal stresses. The tensile simulation is under fully periodic boundary conditions using the NPT ensemble (constant number of particles, pressure, and temperature) and the temperature is maintained at 300 K (room temperature). The maximum tensile strain is 45% in this study, and the loading rate for the tensile simulation is set at $5 \times 10^8 \text{ s}^{-1}$. This loading rate is commonly employed in literature [70]. The stress values in directions other than the tensile direction are maintained at 0.

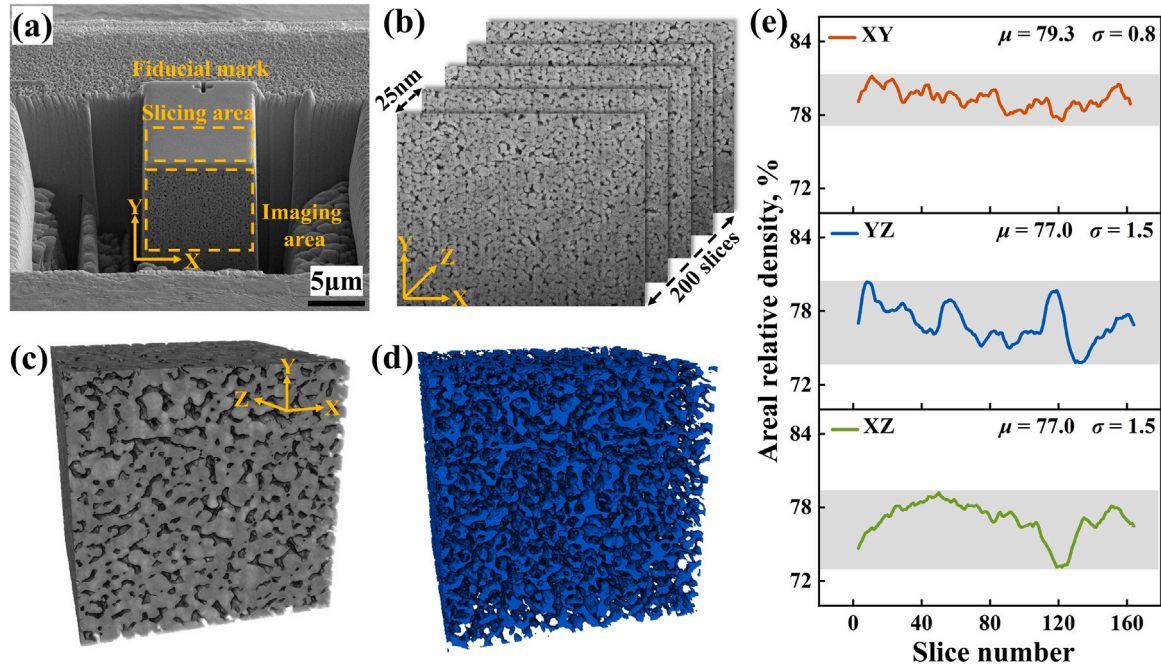


Fig. 4. (a) FIB-SEM tomography image showing the slicing and imaging areas; (b) stacked SEM slices illustrating the consecutive slicing process; (c) sintered Cu NPs domain; (d) porous domain; (e) areal relative density in different directions.

3. Anisotropy in structural evolution during sintering

3.1. Areal relative density by FIB-SEM

Fig. 4(a) presents the image of the slicing and imaging area under FIB-SEM tomography. The dimension of the imaging area is around $10 \times 8 \mu\text{m}^2$ and the depth is around $4.5 \mu\text{m}$. To obtain reliable and representative results, it is crucial to estimate the minimum volume size that must be reconstructed. The critical volume size, which is commonly called a representative volume element (RVE) or stochastic equivalent representative volume element (SERVE), has been extensively discussed in [71–75]. Given that the width and thickness of the micro-cantilevers are near $4 \mu\text{m}$, the reconstructed volume of $4 \times 4 \times 4 \mu\text{m}^3$ is large enough to depict the real microstructure of sintered Cu NPs. 3D reconstruction was carried out by Avizo (Thermo Scientific) after serial image acquisition, which entailed alignment, image processing, and segmentation. Fig. 4(b) shows the image sequence generated via FIB-SEM. Once imaging is done, FIB milling can remove another layer of material using the same parameters to obtain a second image with SEM. By repeatedly performing this milling and imaging process, a 3D dataset of SEM images is created, with each image depicting a 25 nm thick section of the sintered Cu NPs. 200 images were obtained, and around 160 high-resolution images were used to finish the 3D construction. The ‘thresholding’ method was applied in this study [76,77]. The optimal thresholds for the reconstruction were selected by comparing reconstructed models with the morphology of voids in SEM. Figs. 4(c) and (d) represent the sintered Cu NPs and the void volume, respectively.

Here, we define areal relative density as

$$D_r^{\text{areal}} = \frac{A^{\text{matter}}}{A^{\text{cross-section}}} \times 100\%, \quad (1)$$

where A^{matter} and $A^{\text{cross-section}}$ are the area of the sintered Cu NPs domain and the cross-section, respectively. The areal relative density and its mean (μ) and standard deviation (SD, σ) of the 3D reconstructed model along different directions are measured, as shown in Fig. 4(e). The XY plane is perpendicular to the pressure, while the YZ and XZ planes are parallel to the pressure. For the SD of areal relative density, a significantly lower SD (0.8%) is obtained on XY cross-section, compared with 1.5% of YZ and XZ cross-sections. Meanwhile, the XY cross-section

has a minimum areal relative density of 78%, which is greater than that of the YZ (73%) and XZ (74%) cross-sections. It is evident that the areal relative density of the porous structure is anisotropic. Therefore, pressure direction leads to a more uniform distribution of areal relative density, with a relatively high minimum area of cross-section compared to the other two directions.

3.2. Areal relative density by simulation

The sintered structures obtained from the MD simulation are referred to Figs. 3(c) and (d). The final volumetric relative densities for models after simulated sintering is $67.4 \pm 0.7\%$ (under HS), and $68.3 \pm 1.7\%$ (under US). The density is slightly lower than that for experiments because of the limitations of MD simulations on time scales. As for the microstructure, the spherical shape of the particles is preserved after sintering and numerous sintering necks are formed. The majority of pores remain interconnected and the growth and merging of grains are not significant (as evidenced by the minimal change in grain count before and after sintering). The simulated structures are very similar to those reconstructed with FIB-SEM, as shown in Fig. 4(c), illustrating the reliability of this modeling approach. Since the atomic position in the model is discrete, the model is divided into slices with a thickness of 2 \AA (about $1/30$ of the average particle diameter) along the observation direction to calculate areal relative density. Within each slice, the ratio of the number of atoms to the volume of the slice is calculated, and this ratio is then scaled by the atomic density in a dense cubic Cu. Therefore, the areal relative density is defined as

$$D_r^{\text{areal}} = \frac{N^{\text{slice}} \nu^{\text{atom}}}{\nu^{\text{slice}}} \times 100\%, \quad (2)$$

where $N^{\text{slice}} \nu^{\text{atom}}$ is the number of atoms inside the slice of the model. ν^{slice} and ν^{atom} is the volume of the slice and a single Cu atom in FCC crystal ($a = 3.615 \text{ \AA}$), respectively. Our tests show that this slice thickness can capture structural variations without being excessively sensitive, for example, to the influence of grain orientation.

To investigate the effect of the sintering method on the areal relative density distribution, we calculated the areal relative density distribution along different directions for sintered models obtained from the same particle model by different sintering methods. Fig. 5(a) is

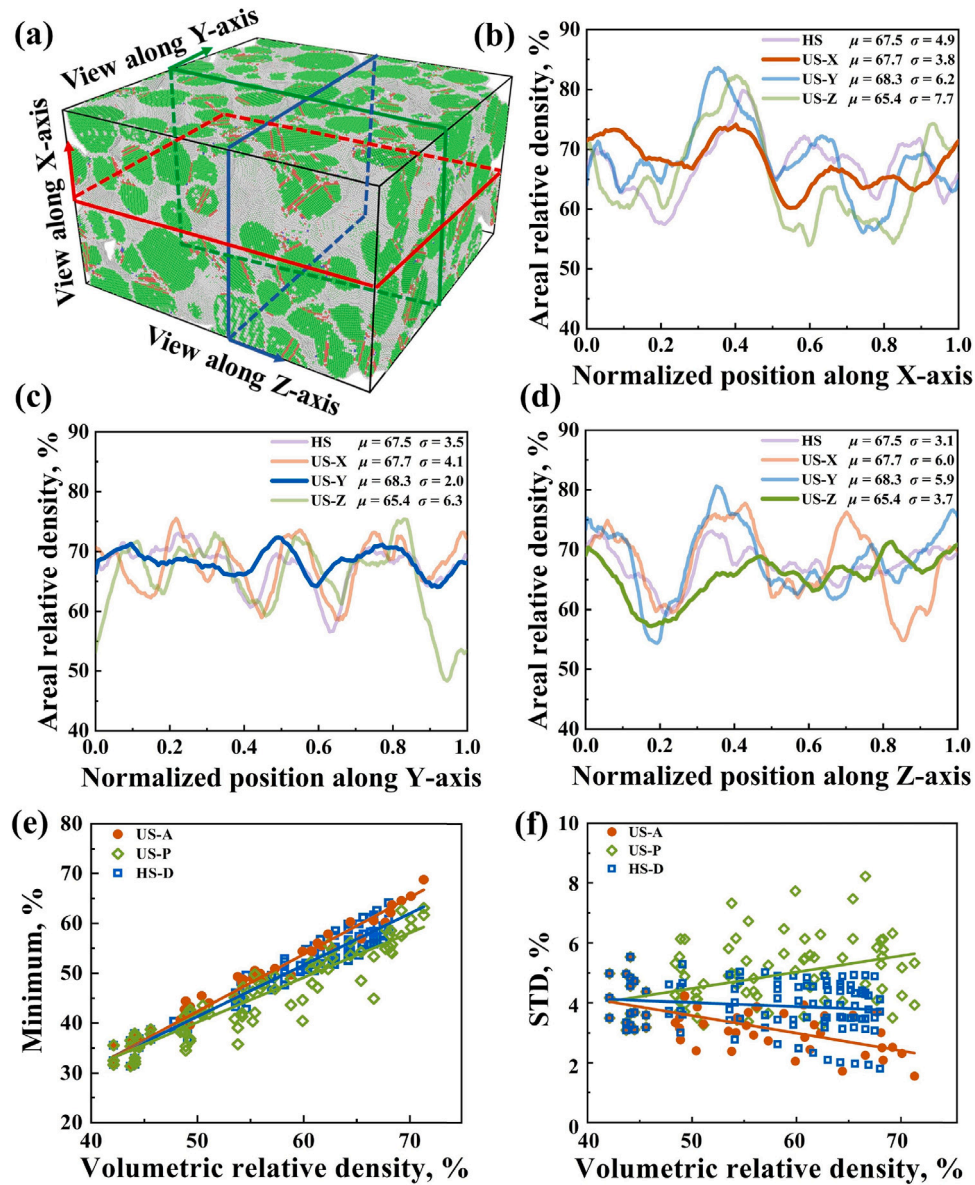


Fig. 5. (a) Sintered model showing the orientations of cross-sections for measuring the areal relative density; (b–d) the changes of areal relative density with position along (b) X-axis, (c) Y-axis and (d) Z-axis under four different sintering conditions, namely, hydrostatic stress (HS) and uniaxial stress (US-X, US-Y, US-Z); (e) the minimum areal relative density versus volumetric relative density; (f) the SD of areal relative density versus volumetric relative density.

the schematic diagram of the view direction for measuring the areal relative density.

Figs. 5(b–d) show the changes of areal relative density along three directions, i.e. X, Y, and Z-axis. Each figure contains four curves corresponding to four sintering methods, i.e. under hydrostatic stress (HS) and uniaxial stress along the X, Y, and Z-axis (US-X, US-Y, and US-Z, respectively). Curves corresponding to US-A, which means for the model the observation direction is consistent with the direction of the stress during sintering, are with deeper color. The normalized coordinates are used as the horizontal axis due to the inconsistent dimensions of the sintered models. Three findings can be drawn from Figs. 5(b–d).

First, a certain degree of heritability in the location of the peaks and troughs of the curves is observed in areal relative density. That means for the same particle model sintered using different methods, when observing along the same direction, the positions of the peaks and valleys of areal relative density curves still exhibit a certain correspondence (although the relative height changes are different), showing the influence of the particle initial packing.

Second, the cross-sections in the US-A direction consistently exhibit a smaller SD and a higher minimum areal relative density value than those of cross-sections in the US-P direction for US models. That means during the sintering process, along the stress direction, the low-density regions caused by the random packing of particles are effectively filled. Surprisingly, US-A curves show lower peaks than US-P curves, indicating particles in high-density regions become more dispersed in the sintering direction. Close inspection of the atomic displacement reveals that due to higher strain and stress in the loading direction, particles require greater displacement along this axis to connect with other particles and bear the load, while along other directions particles have lower driven force for movement.

Third, the cross-sections in HS models generally show intermediate values between those of US-A and US-P for both areal relative density SD and minimum areal relative density. The deviation from the general trend, where the cross-sections of HS model exhibit a lower SD of areal relative density than US-A along the Z-direction, can be attributed to the low areal relative density of the US model compared to the HS model.

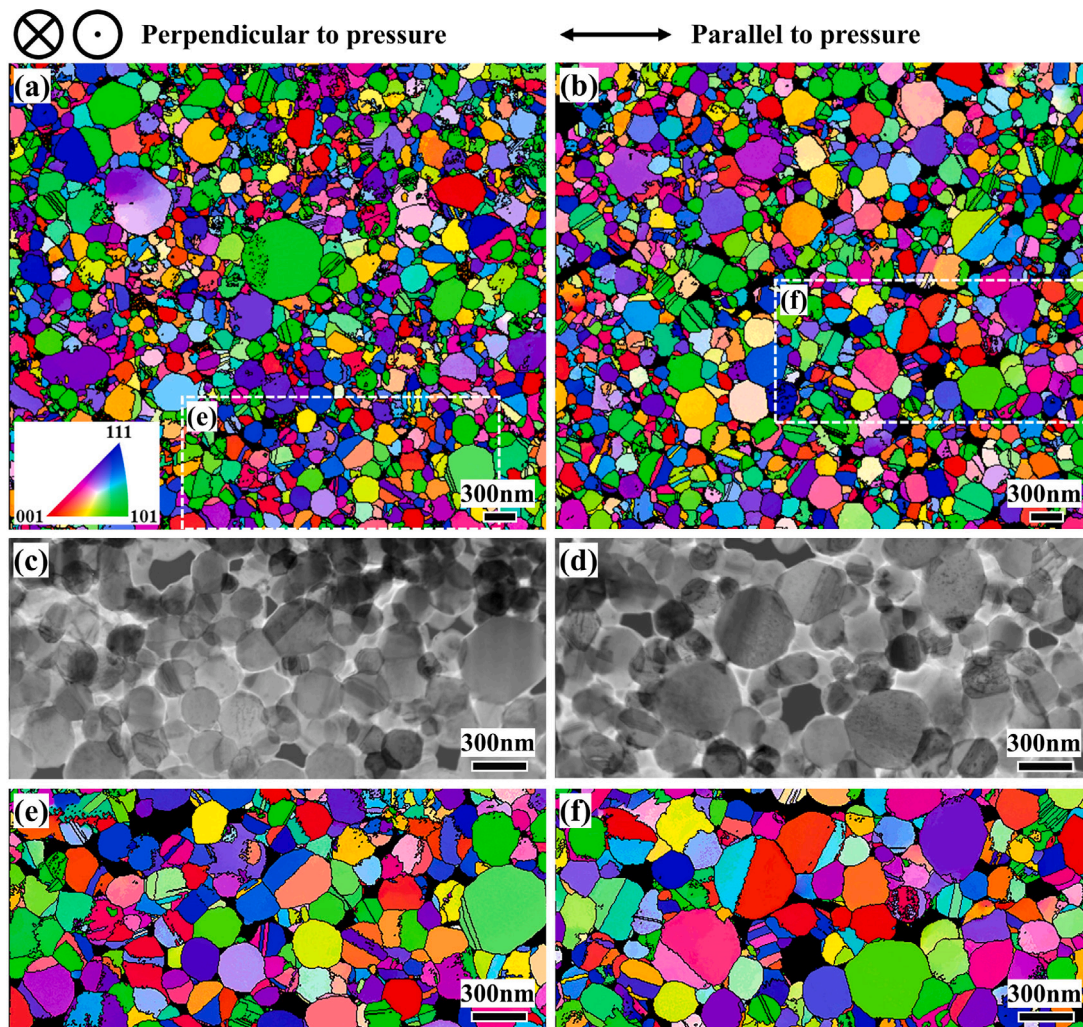


Fig. 6. PED analysis of sintered Cu NPs under external pressure: (a) Grain orientation map of the TEM sample aligned perpendicular to the sintering pressure, corresponding to the 90° micro-cantilevers; (b) grain orientation map of the TEM sample aligned parallel to the sintering pressure, corresponding to the 0° micro-cantilevers; (c, d) virtual bright-field images of the dashed regions in (a) and (b), respectively, revealing local grain morphology; (e, f) corresponding orientation maps of the local regions shown in (c) and (d), respectively.

In order to quantitatively characterize the changes in these structures during sintering, we calculated the minimum values and SD of areal relative density of cross-sections along different directions for each model at various time points during the sintering process, as depicted in Figs. 5(e) and (f).

We found that as the bulk density rises during sintering, the minimum value of the areal relative density rises linearly. The slope of the fitted line for US-A in minimum areal relative density is slightly higher than that for US-P. The case of HS-D is between US-A and US-P. However, for SD of the areal relative density, the tendency is distinctly different for different sintering conditions and observation directions. For the US-A direction, the SD decreases with the increase in bulk density. In contrast, the SD of cross-sections in the US-P direction increases with the rise in bulk density, indicating amplification of structural fluctuations along the direction perpendicular to the applied stress during the sintering process. For HS-D, SD remains nearly constant, implying that the fluctuations in the structure across different directions are at the same magnitude during sintering. Both the two properties along the US-P direction exhibit larger fluctuations than those for US-A, suggesting a more significant influence from the initial particle packing. The fluctuation range for HS-D falls between these two cases.

3.3. Grain orientation characterization

To investigate the effect of sintering pressure on grain orientation and void distribution, two TEM samples were fabricated from the sintered Cu NPs layer. One TEM sample was extracted perpendicular to the sintering pressure direction, aligning with the orientation of the 90° micro-cantilevers. The other one was extracted parallel to the sintering pressure direction, corresponding to the 0° micro-cantilever orientation. Additional details regarding the fabrication of TEM samples are provided in Fig. S1. PED analysis was subsequently performed to characterize the grain orientation maps and void distributions of the two samples. The results are presented in Fig. 6. Figs. 6(a) and (b) depict the grain orientation maps for the perpendicular and parallel directions, respectively. The PED analysis demonstrates that the grain orientation shows no significant dependence on the applied sintering pressure. However, clear anisotropy is observed in the void morphology and particle deformation. In the perpendicular direction (Figs. 6(c, e)), the voids appear irregular and smaller, reflecting localized densification with minimal particle elongation. Conversely, in the parallel direction (Figs. 6(d, f)), the voids are larger and elongated, which can be attributed to the deformation of particles under uniaxial stress during sintering. The external pressure facilitates particle flattening and void coalescence along the loading direction, leading to an anisotropic

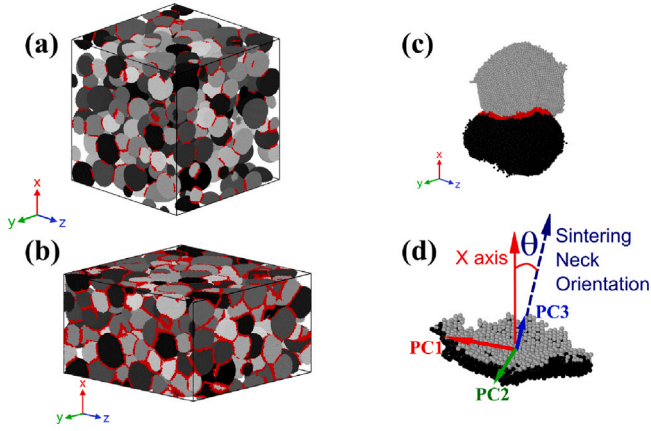


Fig. 7. Neck regions in MD simulation for (a) model before sintering and (b) model sintered under stress along X -axis; (c) a neck between two particles after sintering; (d) principal component analysis for atoms location in a neck. The orientation is quantitatively calculated as the angle between the third principal component and X -axis.

void structure. These observations align with the findings discussed in Sections 3.1 and 3.2, where the pressure direction enhances the uniformity of areal relative density while reducing structural fluctuations. Specifically, the lower standard deviation of relative density along the pressure direction indicates a more stable and homogeneous microstructure. In contrast, the larger density fluctuations in the perpendicular direction reflect the significant influence of initial particle packing and localized void formation.

3.4. Formation of necks during sintering

The fusion between the particles plays an important role in the densification process. According to Ref. [78], the contact area between two particles is considered the sintering neck. In MD models, if atom A, belonging to particle P_A , is within the cutoff distance of atom B, which belongs to particle P_B , then both atom A and B are considered part of the sintering neck between P_A and P_B . The cutoff distance is set to 3.5 Å to ensure that all sintering necks are sufficiently large for meaningful measurement. Using this method, the shape of the necks before and after sintering under stress along the X -axis is shown in red in Figs. 7(a) and (b), respectively. Different particles are distinguished by different shades of gray. The shrinkage along the X -axis after sintering is about 40%. A significant rise in the number and volume of neck regions can be observed. After sintering, the fractions of atoms that were labeled as “neck” increased from 4.6% to 14.8%. Moreover, the necks are interconnected to form a 3D network after sintering is completed, which is beyond the 2D model used in previous simulations of sintering.

To further determine the orientation of each sintering neck, the positions of the atoms for a single sintering neck are extracted, as shown in Fig. 7(c). We consider the neck to be a thin sheet with a significant difference between thickness and area, with the thickness direction representing the orientation of the neck. Using principal component analysis (PCA), the three orthogonal principal component (PC) vectors for the atomic positions are determined. The plane defined by PC1 and PC2 is the plane with the most dispersed atomic coordinates. PC3, which is perpendicular to this plane, is the direction with the least atomic dispersion, indicating the orientation of the sintering neck. Fig. 7(d) is a schematic diagram for calculating the angle θ between the neck orientation (PC3) and the X -axis. It is clear that when θ approaches 0, the neck is perpendicular to the given axis, while θ near 90° means the neck is parallel to the given axis.

It is important to note that, mathematically, the distribution of the angle of a random vector in 3D space with a specific vector is not

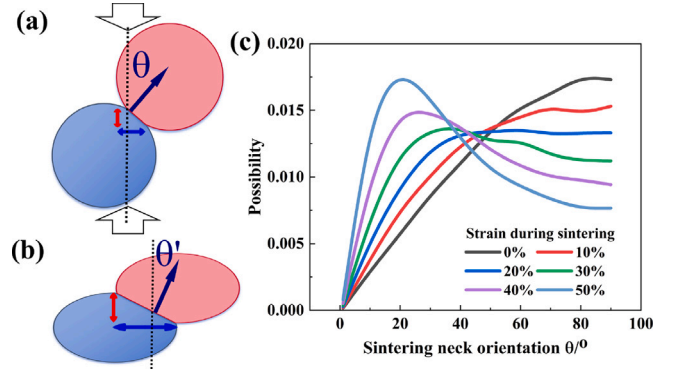


Fig. 8. Schematic illustration of the effect of particle deformation on sintered neck orientation: (a) Two particles with initial contact before sintering; (b) a neck formed between two deformed particles; (c) distribution of θ for particles with various strain during sintering derived from the 2D model.

uniform. It is trivial to prove that for angle θ ranging in 0 to 90°, the probability density function $F(\theta)$ of the angle between a random vector and a fixed vector is

$$F(\theta) \propto \sin(\theta). \quad (3)$$

Thus there is a much higher possibility for a vector to be perpendicular to a specific axis, rather than parallel to that.

A DEM study of ceramic sintering showed that the anisotropy flattening under stress has a substantial contribution to structure anisotropy [33]. Since the sintering of metal NPs is featured by low sintering temperature and short sintering time, the anisotropy induced by particle deformation is expected to be more significant. Here we use a 2D schematic to illustrate the effect of deformation caused by the uniaxial stress on the orientation of the neck formed during sintering. Fig. 8(a) shows two particles before sintering. θ is the angle between the normal of the initial contact surface and the stress direction. Here,

$$\tan \theta = \frac{a}{b}, \quad (4)$$

where a and b are the dimensions of the initial sintering neck in the parallel and perpendicular directions to the loading, respectively. After uniaxial stress-assisted sintering, the particle shape significantly contracts along the direction of the uniaxial stress with a strain of ϵ , while Poisson expansion occurs in the other directions, as shown in Fig. 8(b). The neck also grows during sintering. Then θ' can be estimated as

$$\tan \theta' = \frac{k \cdot a(1 - \epsilon)}{k \cdot b(1 + \nu\epsilon)}, \quad (5)$$

where k describes the uniform growth of the sintering neck dimensions in all directions, and ν is the Poisson's ratio of the bulk material. It should be noted that the strain during sintering should be smaller than the shrinkage deformation along the stress direction, as both particle deformation and densification contribute to the shrinkage. Using this method, the orientation distributions of necks considering particle deformation are calculated, as shown in Fig. 8(c). The black curve, which is for particles before deformation, corresponding to the distribution described by Eq. (3). The peak of angle distribution significantly shifts to low angle region as particle strain increases, meaning that after large deformation, necks tend to be perpendicular to the stress direction geometrically.

The orientations of the necks in the MD models sintered under stress along the X -axis are analyzed. The US-X with deformation of 40% (Figs. 9(a–c)) and 50% (Figs. 9(d–f)) contain 742 and 883 necks, respectively. The model with 50% deformation is analyzed here to better show the effect of uniaxial compression during sintering on the microstructure. Figs. 9(a, d), (b, e), and (c, f) are for the neck

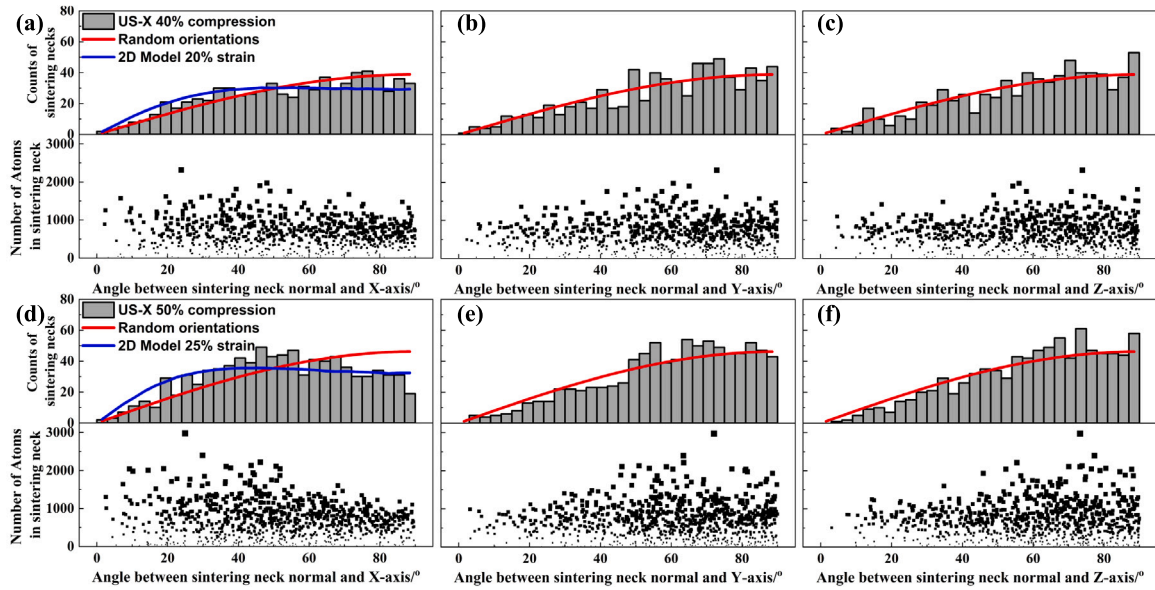


Fig. 9. Statistics on sintering necks orientation (histograms) and size (scatter plots). (a–c) are for model with 40% deformation and (d–f) are for model with 50% deformation along X -axis during sintering. The angle shown in (a, d), (b, e), and (c, f) are between neck normals and X -, Y -, and Z -axis, respectively. Red reference curves show the angle distribution for randomly oriented vectors. Blue lines are derived from Eq. (5).

orientations with respect to X -, Y -, and Z -axis, respectively. In each figure, the histogram counts the number of necks with different angles to the axis. The scatter plot shows the number of atoms contained in the necks with different orientations. The size of marks in scatter plots is also adjusted according to the number of atoms. The distribution curves for the angles between randomly oriented vectors to the axis (Eq. (3)) are shown with a red solid line in each histogram for reference. In Figs. 9(a) and (d), the distribution of the neck orientations derived from Eq. (5) are shown in blue curves. In the calculation, the strain of each particle is considered as half of the deformation along the X -axis and $\mu = 0.3$.

Three points can be drawn from the figure.

1. For the orientation of necks concerning the direction of the uniaxial stress, here X -axis, the histogram shows that the number is higher between 0° and 50° than the reference line. For the orientation of the sintered neck along the Y and Z axes, the number is higher near 90° . This indicates that along the X -axis, more sintered necks are present perpendicular to the X -axis or at an angle of less than 50° , while in the other two orientations, most of the sintered necks are close to parallel to this orientation.

2. Large dots in the scatter plots corresponding to the X -axis are clustered in the angle range of 10° to 45° , while for the plots of the Y - and Z -axis, the dots representing a larger number of atoms are clustered in the range of 60° to 90° . This suggests that sintered necks oriented close to perpendicular to the stress direction (here the X -axis) grow larger (compared to those parallel to the X -axis).

3. By comparing models experiencing 40% versus 50% deformation, the effect of deformation strain on the formation and growth of necks is revealed. With extra 10% compression, both the number and size of necks at an angle of 20° to 50° to the X -axis rise significantly, while there is no such tendency for the Y - and Z -axes.

The orientation of the sintered necks mainly originates from the flattening of the particle shape under uniaxial stress. In Ref. [33], the authors state that the particle flattening induced by uniaxial stress is anisotropic, with particles having a larger size and surface area perpendicular to the stress direction. The trend can be seen by comparing Fig. 6(a) and (b). The difference between the solid blue line and the actual distribution is mainly caused by the non-uniform strain distribution during sintering. Another reason for the distribution of neck orientations is the high body shrinkage along the direction of the sintering stress. Along the direction of the stress, the particles have more opportunities to contact each other thus more necks form.

4. Mechanical properties of sintered NPs and discussion

4.1. Micro-cantilever bending tests

Due to the limitations of FIB in preparing specimens with different orientations, the cross-section of the cantilever beam in this study is not rectangle. In our previous work, the fracture toughness of sintered Cu NPs was measured with standard micro-cantilevers as $3.2 \text{ MPa m}^{1/2}$ [31], which aligns well with other reports [29]. Figs. 10(a–c) show the load–displacement curves obtained from micro-cantilever bending tests. The initial elastic loading parts matched well across specimens, but some scatter appeared at larger displacements due to slight differences in sample dimensions. The maximum load values F_{\max} were retrieved from the peak points of the load–displacement curves. As depicted in Fig. 10(d), the maximum load and SD of 0° , 45° , and 90° micro-cantilevers are $203 \pm 20 \text{ }\mu\text{N}$, $266 \pm 68 \text{ }\mu\text{N}$, and $286 \pm 36 \text{ }\mu\text{N}$, respectively. Since the specimens are essentially the same size, F_{\max} is proportional to the fracture strength. The 90° micro-cantilevers, in which the prefabricated notch is perpendicular to the uniaxial stress during sintering, show 41% higher strength than 0° micro-cantilevers. The 45° micro-cantilevers exhibit slightly lower strength than the 90° micro-cantilevers, and the values are dispersed in a large range. The slopes of the load–displacement curves indicate the degree of densification of the specimen in the loaded direction, so we also calculated the slopes as the effective modulus. For 0° , 45° , and 90° micro-cantilevers, the modulus are $0.32 \pm 0.04 \text{ }\mu\text{N nm}^{-1}$, $0.42 \pm 0.06 \text{ }\mu\text{N nm}^{-1}$, and $0.45 \pm 0.05 \text{ }\mu\text{N nm}^{-1}$, respectively. The value for 90° micro-cantilevers is slightly higher than that for 45° micro-cantilevers, and significantly higher than that for 0° micro-cantilevers. Intuitively, we expect the mechanical property of 45° micro-cantilevers to be between those of 0° and 90° , following the rule of mixtures. The high toughness measured on 45° micro-cantilevers which is beyond expectation will be discussed in Section 4.3.

4.2. Toughness from MD simulation

Three independent sintering models were used for the simulations, resulting in nine MD models subjected to uniaxial stress and three models to hydrostatic stress. Tensile simulations were then conducted in the X , Y , and Z directions for the nine sintered models, generating

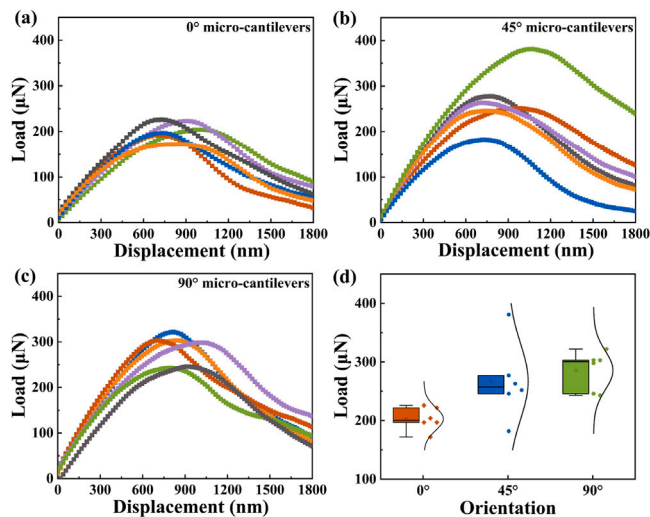


Fig. 10. Load-displacement curves of (a) 0°, (b) 45°, (c) 90° micro-cantilevers; (d) maximum loads of micro-cantilevers with different orientations.

27 stress-strain curves. For the three models sintered under hydrostatic stress, the tensile tests produced nine stress-strain curves.

To characterize the microstructure and mechanical behavior, we use a model sintered under a stress along the *X*-axis as an illustrative example, shown in Fig. 11(c). The models under 40% tensile deformation along the *X*, *Y*, and *Z* axes are depicted in Figs. 11(a–c), respectively. Fracture is observed in the models stretched along the *Y* and *Z* axes, which is also reflected in the stress-strain curves (Fig. 11(d)). The curve corresponding to tensile stress along the *X*-direction shows higher tensile strength than those for the *Y* and *Z* directions, matching well with experimental results. The toughness of the sintered Cu NPs models is related to the areas under the stress-strain curves, calculated as follows:

$$G_f = \int_0^{\epsilon_f} \sigma d\epsilon, \quad (6)$$

where ϵ_f is the strain corresponding to failure and σ is the tensile stress [79]. The toughness here indicates the capacity for energy absorption during plastic deformation, not the fracture toughness. The unit for toughness is MPa or MJ m⁻³.

The fracture toughness estimated from the 36 stress-strain curves is connected to features of areal relative density. Fig. 11(f) illustrates that toughness increases rapidly when the minimal areal relative density exceeds 60%. Even with similar minimal areal relative density, the toughness for tensile stress along the sintering direction (US-A) is much higher than that for US-P and HS-D. In Fig. 11(g), directions with smaller SD exhibit higher toughness. Moreover, a small SD value indicates a small variance in toughness. A direct comparison of toughness for US-A, US-P, and HS-D is shown in Fig. 11(h). Along the direction of sintering stress (US-A), the toughness is twice that of US-P. The toughness of HS-D is close to the average values in the three directions of the model sintered under uniaxial stress.

4.3. Effect of microstructural anisotropy on mechanical performance

Experimental and MD simulations reveal the anisotropy of the sintered structure in terms of surface density distribution and sintering neck orientation. The influence of the minimal areal relative density on mechanical properties is evident. Under uniform deformation, locations with small cross-sections are prone to stress concentrations, akin to the necking observed in general tensile deformation. Moreover, since Cu NPs are at the nanoscale, dislocation generation and multiplication are suppressed, and work hardening can hardly contribute to

the strength of regions with high strain. Thus, strain localization at cross-sections with small areas is self-promoting, limiting mechanical performance. Long et al. [80] proved the effect of strain localization on the mechanical properties of sintered NPs.

For a homogeneous dense structure, stress concentration is bound to occur at the minimum areal relative density. For sintered Cu NPs, however, the stress distribution under uniform strain is strongly dependent on the porous structure and the position with minimal area is not necessarily the most dangerous region. It can be proved by the MD simulation of the tensile process of sintered Cu NPs. The initiation positions for fracture are labeled on the areal relative density curves (Fig. S2). It is found that fracture does not always occur at the cross-section with minimal areal relative density. SD is not sensitive to extreme values but describes the homogeneity of the material distribution for porous structures, complementing the minimal areal relative density. For structures with similar bulk relative densities, those with smaller SD have a lower possibility for strain localization and thus better mechanical properties. This conclusion is also supported by FEM [81] and phase field [82] simulations of tensile deformation of porous structures.

In other studies, it has been observed that the aspect ratio of pores increases after sintering and pores mainly align along the direction of the stress. The presence of elongated pores along the stress direction leads to smaller fluctuations in areal relative density in that direction compared to larger fluctuations in other directions. Therefore the anisotropy of pore shape reported before is consistent with the differences in directional SD of areal relative density we observed. For 3D interconnected pores, as shown by the 3D reconstruction, 2D interface observation is insufficient to fully display their characteristics. Here, we point out that SD of areal relative density is a reliable indicator for the quantitative description of 3D porous structures. Additionally, using SD as a measurement provides an alternative explanation for the size effect of porous structures [83]. For the same pore distribution, the areal relative density of smaller samples is more significantly affected by the pores, resulting in a higher SD. Multiple reports indicate that after high-temperature aging, accompanied by an increase in pore size, the mechanical properties of sintered Ag decline even if the relative density remains unchanged or increases. This is also consistent with the conclusions drawn here.

From another perspective, the anisotropy of sintered NPs can be explained by difference of failure mode. In the experiments conducted in [84], two primary failure modes were observed: tensile fracture and shear fracture. Since the necks are the weakest regions in the material, it can be inferred that the failure mode is related to the orientation of these necks. Due to the good plasticity of Cu, the fracture surfaces in the micro-cantilever bending tests did not completely separate, allowing only the observation of the fracture surfaces, which are shown in the Fig. S3.

In MD simulations, these two fracture modes are also observed. For the model sintered under stress along the *X*-axis, the typical fracture surfaces during tensile deformation along *X*-axis (US-A) and *Y*-axis (US-P) are shown in Figs. 12(a) and (b), respectively. Atoms from different particles are color-coded, and the overall deformation of the model is indicated below each image. The total deformation along the tensile direction at 30% strain is marked on each particle. On the right side, the atomic structures before and after 30% deformation are shown, analyzed using CNA, with the surface amorphous layer removed for clarity. Red indicates the hexagonal closest packed (HCP) structure, corresponding to stacking faults in Cu.

In Fig. 12(a), the sintering neck is almost perpendicular to the tensile direction, resulting in uniform deformation across the particles (each particle contains many stacking faults), indicating tensile fracture. In Fig. 12(b), the sintering neck is nearly parallel to the tensile direction, resulting in significantly higher deformation in the green particle compared to the overall deformation value, while the red particle shows less deformation. At the fracture site, many atoms

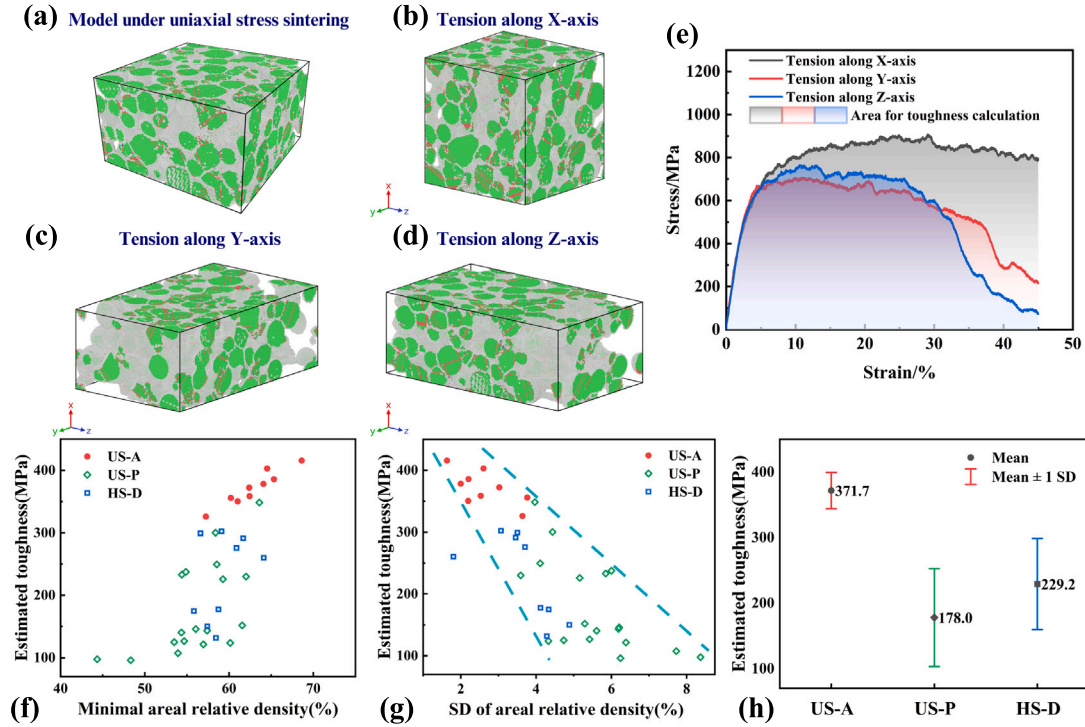


Fig. 11. (a) Cu NPs model sintered under uniaxial stress along the X-axis. Atoms are colored according to its local structure; (b–d) sintered model after 45% tensile deformation along (b) X-axis, (c) Y-axis and (d) Z-axis; (e) stress–strain curves for tensile deformation along the three axes. The shaded area under each curve was used to calculate the tensile toughness. Two features describing the microstructure are connected with the estimated toughness: (f) minimum and (g) standard deviation of areal relative density. (h) Toughness for tensile along different directions. US-A(US-P) refer to the direction along(perpendicular) to the stress direction during sintering. HS-D refers to models sintered under hydrostatic stress. The dash lines in (g) are guide to eyes.

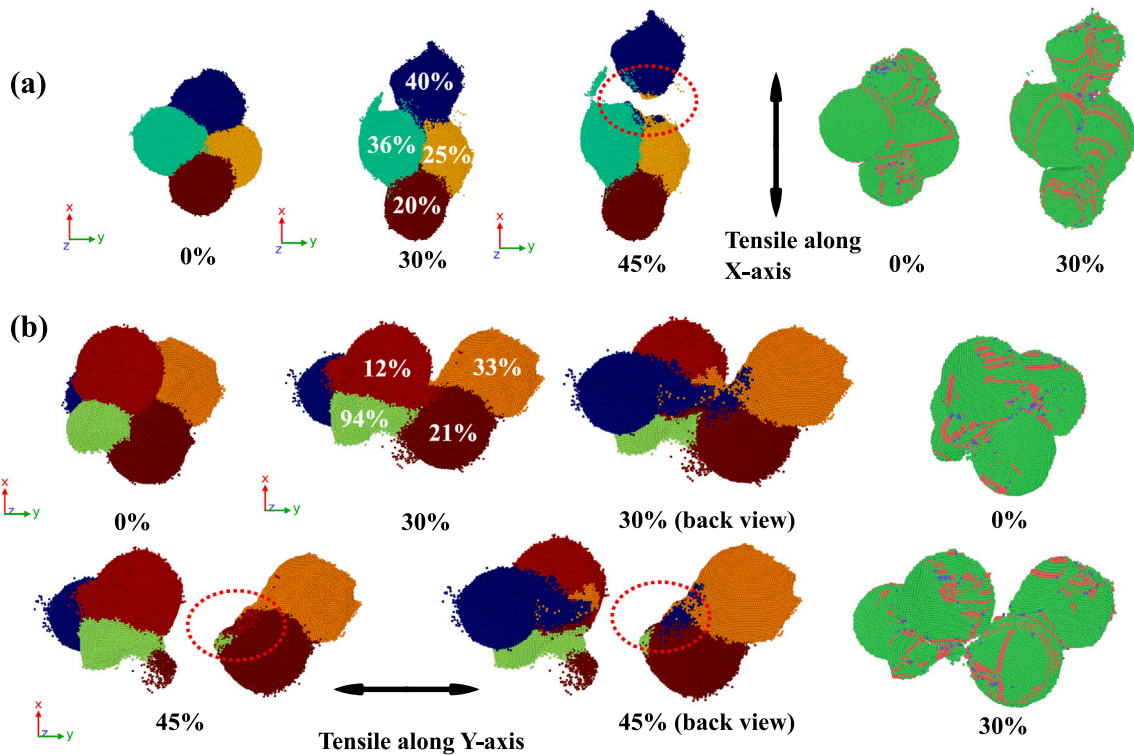


Fig. 12. The fracture process during tensile deformation along (a) X-axis and (b) Y-axis. The model is sintered under stress along X-axis. Atoms are colored according to the particle they belong to. Left side shows the atomic structure with common neighbor analysis (CNA).

adhere to other particles, suggesting the fracture is by shearing at the neck.

Considering a sintering neck with an orientation angle θ and area A , as shown in Fig. 8, when stretched along the direction of sintering stress, its effective bearing area is $A \cos \theta$. When stretched in the vertical direction, the effective bearing area is $A \sin \theta$. Moreover, for necks with θ varying from 0 to 90°, the stress state on the neck plane changes from pure tension to pure shear, which lead to a transition in fracture mode. Thus, geometrically, sintering necks with a smaller angle between the normal and tensile direction are more advantageous. Given the observed anisotropy in the orientation of sintering necks after sintering, θ angles of sintering necks observed along the X -axis are more likely to be smaller, leading to better mechanical performance when stretched along the X -axis.

In the micro-cantilever bending tests, the 45° specimens exhibited strength close to that of the 90° specimens. Considering that the orientation distribution of sintering necks has a peak at 45°, it can be inferred that when stretched at a 45° angle to the sintering stress direction, many necks align favorably, resulting in better performance.

Due to the complexity of the sintered particle structure, the effects of areal relative density fluctuations, sintering neck orientation, and other factors not considered (such as grain boundary types and grain orientations) are superimposed.

5. Conclusion

The mechanical strength of sintered NPs limits their application in advanced electronics packaging. In this work, we reveal the anisotropy in the microstructure and mechanical properties of sintered Cu NPs by combining experimental methods with MD simulations. We clearly explain the processing-microstructure-property relationship of pressure-assisted sintered Cu NPs. The main findings are as follows:

1. The evolution of the microstructure during sintering is quantitatively described by areal relative density, which shows distinct differences in each direction during stress-assisted sintering. Directions along the stress exhibit a quick decrease in the minimum and SD of areal relative density, while directions perpendicular to the stress show an increase in SD. For sintering under hydrostatic stress, changes in all directions are similar.
2. MD simulations reveal that the necks formed during sintering are anisotropic. Necks tend to attain a smaller angle between their normal and the stress direction. Additionally, necks with such favorable orientation can achieve larger sizes.
3. The anisotropy in the mechanical properties of Cu NPs sintered under uniaxial stress is demonstrated by both micro-cantilever bending tests and tensile simulations. Along the direction of the sintering stress, the strength (load in experiments and toughness in simulations) is significantly higher (41% in experiments and 108% in simulations) than that along the perpendicular directions.
4. The mechanical anisotropy is induced by the microstructure through two aspects: variations in areal relative density affect the tendency for strain localization, and the size and orientation of necks affect the fracture mode. Along the direction of the sintering stress, the structure is more uniform, and more necks are in favorable orientations, resulting in higher strength compared to other directions.

We expect this study to provide new insights for nanoscale experimental design and performance analysis, as well as inform the design of NPs sintering processes.

CRediT authorship contribution statement

Leiming Du: Writing – original draft, Methodology, Investigation, Conceptualization. **Kai Liu:** Writing – original draft, Software, Methodology. **Dong Hu:** Methodology, Investigation. **Olof Bäcké:** Validation, Methodology. **Xiao Hu:** Methodology. **Xinrui Ji:** Methodology. **Jiajie Fan:** Writing – review & editing, Supervision. **René H. Poelma:** Writing – review & editing, Writing – original draft, Supervision. **Magnus Hörnqvist Colliander:** Writing – review & editing, Supervision. **Guoqi Zhang:** Writing – review & editing, Supervision.

Declaration of competing interest

All authors disclosed no relevant relationships.

Acknowledgments

The authors would like to acknowledge the financial support from the ECSEL Joint Undertaking (JU) under grant agreement No 876659. The JU receives support from the European Union's Horizon 2020 research and innovation program and Germany, Austria, Slovakia, Sweden, Finland, Belgium, Italy, Spain, Netherlands, Slovenia, Greece, France, and Turkey.

Appendix A. Supplementary data

Supplementary material related to this article can be found online at <https://doi.org/10.1016/j.actamat.2025.120772>.

References

- [1] C.R. Eddy Jr., D.K. Gaskill, Silicon carbide as a platform for power electronics, *Science* 324 (5933) (2009) 1398–1400.
- [2] Cyril Buttay, Dominique Planson, Bruno Allard, Dominique Bergogne, Pascal Bevilacqua, Charles Joubert, Mihai Lazar, Christian Martin, Hervé Morel, Dominique Tournier, et al., State of the art of high temperature power electronics, *Mater. Sci. Engineering: B* 176 (4) (2011) 283–288.
- [3] Yue Gao, Shuhei Takata, Chuantong Chen, Shijo Nagao, Katsuaki Suganuma, Amir Sajjad Bahman, Francesco Iannuzzo, Reliability analysis of sintered Cu joints for SiC power devices under thermal shock condition, *Microelectron. Reliab.* 100 (2019) 113456.
- [4] A.U. Telang, T.R. Bieler, A. Zamiri, F. Pourboghrat, Incremental recrystallization/grain growth driven by elastic strain energy release in a thermomechanically fatigued lead-free solder joint, *Acta Mater.* 55 (7) (2007) 2265–2277.
- [5] Muhammad Sadiq, Maaz Khan, Abdul Mateen, Muhammad Shahzad, Kareem Akhtar, Jawad Khan, et al., Thermal aging impact on microstructure, creep and corrosion behavior of lead-free solder alloy (SAC387) use in electronics, *Microelectron. Reliab.* 122 (2021) 114180.
- [6] Wenwu Zhang, Penghao Zhang, Dashi Lu, Hao Pan, Xiangli Liu, Chengyan Xu, Jun Wei, Mingyu Li, Hongjun Ji, A supersaturated Cu-Ag nanoalloy joint with ultrahigh shear strength and ultrafine nanoprecipitates for power electronic packaging, *J. Mater. Sci. Technol.* 145 (2023) 56–65.
- [7] Jintao Wang, Ziwen Lv, Luobin Zhang, Fangcheng Duan, Jianqiang Wang, Fuquan Li, Hongtao Chen, Mingyu Li, Nucleation and growth of Cu₆Sn₅ during the aging process of Cu/Sn interface in electronic packaging-by in-situ TEM, *Acta Mater.* 264 (2024) 119581.
- [8] M.A. Asoro, P.J. Ferreira, D. Kovar, In situ transmission electron microscopy and scanning transmission electron microscopy studies of sintering of Ag and Pt nanoparticles, *Acta Mater.* 81 (2014) 173–183.
- [9] SuYan Zhao, Xin Li, YunHui Mei, GuoQuan Lu, Study on high temperature bonding reliability of sintered nano-silver joint on bare copper plate, *Microelectron. Reliab.* 55 (12) (2015) 2524–2531.
- [10] Xu Long, Zhen Li, Xiuzhen Lu, Hongcun Guo, Chao Chang, Qianran Zhang, Abdelhafid Zehri, Wei Ke, Yao Yao, Lilei Ye, et al., Mechanical behaviour of sintered silver nanoparticles reinforced by SiC microparticles, *Mater. Sci. Engineering: A* 744 (2019) 406–414.
- [11] Bowen Zhang, Chuantong Chen, Takuya Sekiguchi, Yang Liu, Caifu Li, Katsuaki Suganuma, Development of anti-oxidation ag salt paste for large-area (35× 35 mm²) Cu-Cu bonding with ultra-high bonding strength, *J. Mater. Sci. Technol.* 113 (2022) 261–270.
- [12] Wei Chen, Xu Liu, Dong Hu, Xi Zhu, Xuejun Fan, Guoqi Zhang, Jiajie Fan, Unraveling the hydrogen sulfide aging mechanism on electrical-thermal-mechanical property degradation of sintered nanocopper interconnects used in power electronics packaging, *Mater. Des.* 238 (2024) 112702.

- [13] Sathish K Kurapati, N Mahendar Reddy, R Sujithra, Ramesh Kola, Gubbala V Ramesh, D Saritha, Nanomaterials and nanostructures in additive manufacturing: properties, applications, and technological challenges, *Nanotechnology- Based Addit. Manufacturing: Prod. Des. Prop. Appl.* 1 (2023) 53–102.
- [14] O. Lame, D. Bellet, M. Di Michiel, D. Bouvard, Bulk observation of metal powder sintering by X-ray synchrotron microtomography, *Acta Mater.* 52 (4) (2004) 977–984.
- [15] Ruzhong Zuo, Emil Aulbach, Rajendra K Bordia, Jürgen Rödel, Critical evaluation of hot forging experiments: case study in alumina, *J. Am. Ceram. Soc.* 86 (7) (2003) 1099–1105.
- [16] David J. Green, Olivier Guillon, Jürgen Rödel, Constrained sintering: A delicate balance of scales, *J. Eur. Ceram. Soc.* 28 (7) (2008) 1451–1466.
- [17] Haixia Shang, Aravind Mohanram, Eugene Olevsky, Rajendra K Bordia, Evolution of anisotropy in hierarchical porous ceramics during sinter-forging, *J. Eur. Ceram. Soc.* 36 (12) (2016) 2937–2945.
- [18] Olivier Guillon, Ludwig Weiler, Jürgen Rödel, Anisotropic microstructural development during the constrained sintering of dip-coated alumina thin films, *J. Am. Ceram. Soc.* 90 (5) (2007) 1394–1400.
- [19] C.L. Martin, R.K. Bordia, The effect of a substrate on the sintering of constrained films, *Acta Mater.* 57 (2) (2009) 549–558.
- [20] Tiam Foo Chen, Kim Shyong Siow, Comparing the mechanical and thermal-electrical properties of sintered copper (Cu) and sintered silver (Ag) joints, *J. Alloys Compd.* 866 (2021) 158783.
- [21] Yang Zuo, Cong Zhao, Ana Robador, Martin Wickham, Samjid H Mannan, Quasi-in-situ observation of the grain growth and grain boundary movement in sintered Cu nanoparticle interconnects, *Acta Mater.* 236 (2022) 118135.
- [22] Toni Youssef, Wafaa Rmili, Eric Woigard, Stephane Azzopardi, Nicolas Vivet, Donatien Martineau, Régis Meuret, Guenael Le Quilliec, Caroline Richard, Power modules die attach: A comprehensive evolution of the nanosilver sintering physical properties versus its porosity, *Microelectron. Reliab.* 55 (9–10) (2015) 1997–2002.
- [23] Bo Chen, Zhenbo Xia, Kathy Lu, Understanding sintering characteristics of ZnO nanoparticles by FIB-SEM three-dimensional analysis, *J. Eur. Ceram. Soc.* 33 (13–14) (2013) 2499–2507.
- [24] Gaku Okuma, Ryo Miyaki, Kan Shinobe, Anna Sciazko, Takaaki Shimura, Zilin Yan, Shotaro Hara, Toshinori Ogashiwa, Naoki Shikazono, Fumihiro Wakai, Anisotropic microstructural evolution and coarsening in free sintering and constrained sintering of metal film by using FIB-SEM tomography, *Acta Mater.* 215 (2021) 117087.
- [25] Aatreya Manjulagiri Venkatesh, Didier Bouvard, Pierre Lhuissier, Julie Villanova, Cyril Rajon, In-situ 3D X-ray investigation of ceramic powder sintering at the particle length-scale, *Ceram. Int.* 50 (3) (2024) 4715–4728.
- [26] Aatreya Manjulagiri Venkatesh, Didier Bouvard, Pierre Lhuissier, Julie Villanova, 3D analysis of ceramic powder sintering by synchrotron X-ray nano-tomography, *J. Eur. Ceram. Soc.* 43 (6) (2023) 2553–2563.
- [27] Pascal Gadaud, Vincenzo Caccuri, Denis Bertheau, James Carr, Xavier Milhet, Ageing sintered silver: relationship between tensile behavior, mechanical properties and the nanoporous structure evolution, *Mater. Sci. Engineering: A* 669 (2016) 379–386.
- [28] Chuantong Chen, Katsuaki Sukanuma, Microstructure and mechanical properties of sintered Ag particles with flake and spherical shape from nano to micro size, *Mater. Des.* 162 (2019) 311–321.
- [29] Chuantong Chen, Shijo Nagao, Katsuaki Sukanuma, Jinting Jiu, Tohru Sugahara, Hao Zhang, Tomohito Iwashige, Kazuhiko Sugiura, Kazuhiro Tsuruta, Macroscale and microscale fracture toughness of microporous sintered Ag for applications in power electronic devices, *Acta Mater.* 129 (2017) 41–51.
- [30] Leiming Du, Dong Hu, René Poelm, Willem Van Driel, Kouchi Zhang, Micro-cantilever bending test of sintered Cu nanoparticles for power electronic devices, in: 2023 24th International Conference on Thermal, Mechanical and Multi-Physics Simulation and Experiments in Microelectronics and Microsystems (EuroSimE), IEEE, 2023, pp. 1–4.
- [31] Dong Hu, Leiming Du, Markus Alfreider, Jiajie Fan, Daniel Kiener, Guoqi Zhang, Microscopic fracture toughness of notched porous sintered Cu micro-cantilevers for power electronics packaging, *Mater. Sci. Engineering: A* 897 (2024) 146316.
- [32] Brayan Paredes-Goyes, David Jauffres, Jean-Michel Missiaen, Christophe L Martin, Grain growth in sintering: A discrete element model on large packings, *Acta Mater.* 218 (2021) 117182.
- [33] A Wonisch, O Guillon, T Kraft, M Moseler, H Riedel, J Rödel, Stress-induced anisotropy of sintering alumina: Discrete element modelling and experiments, *Acta Mater.* 55 (15) (2007) 5187–5199.
- [34] Branislav Dzepina, Daniel Balint, Daniele Dini, A phase field model of pressure-assisted sintering, *J. Eur. Ceram. Soc.* 39 (2–3) (2019) 173–182.
- [35] Johannes Hötzer, Marco Seiz, Michael Kellner, Wolfgang Rheinheimer, Britta Nestler, Phase-field simulation of solid state sintering, *Acta Mater.* 164 (2019) 184–195.
- [36] Robert Termuhlen, Xanthippi Chatzistavrou, Jason D Nicholas, Hui-Chia Yu, Three-dimensional phase field sintering simulations accounting for the rigid-body motion of individual grains, *Comput. Mater. Sci.* 186 (2021) 109963.
- [37] Shota Okuno, Qiang Yu, Yusuke Nakata, Influence of sintering conditions on mechanical properties of Ag-nano sintered material, in: 2016 IEEE 18th Electronics Packaging Technology Conference, EPTC, IEEE, 2016, pp. 488–491.
- [38] Gong He, Guo Hongcun, Li Shujin, Zhou Junwen, Yao Yao, Compressive failure mechanism of sintered nano-silver, *J. Mater. Res.* 38 (18) (2023) 4201–4213.
- [39] Yutai Su, Guicui Fu, Changqing Liu, Kun Zhang, Liguao Zhao, Canyu Liu, Allan Liu, Jianan Song, Thermo-elasto-plastic phase-field modelling of mechanical behaviours of sintered nano-silver with randomly distributed micro-pores, *Comput. Methods Appl. Mech. Engrg.* 378 (2021) 113729.
- [40] Lifeng Ding, Ruslan L. Davidchack, Jingzhe Pan, A molecular dynamics study of sintering between nanoparticles, *Comput. Mater. Sci.* 45 (2) (2009) 247–256.
- [41] Dong Hu, Zhen Cui, Jiajie Fan, Xuejun Fan, Guoqi Zhang, Thermal kinetic and mechanical behaviors of pressure-assisted Cu nanoparticles sintering: A molecular dynamics study, *Results Phys.* 19 (2020) 103486.
- [42] Yanan Hu, Yuexing Wang, Yao Yao, Molecular dynamics on the sintering mechanism and mechanical feature of the silver nanoparticles at different temperatures, *Mater. Today Commun.* 34 (2023) 105292.
- [43] Jingxiang Xu, Yuji Higuchi, Nobuki Ozawa, Kazuhisa Sato, Toshiyuki Hashida, Momoji Kubo, Parallel large-scale molecular dynamics simulation opens new perspective to clarify the effect of a porous structure on the sintering process of Ni/YSZ multiparticles, *ACS Appl. Mater. & Interfaces* 9 (37) (2017) 31816–31824.
- [44] Qingwei Guo, Hua Hou, Kaile Wang, Muxi Li, Peter K Liaw, Yuhong Zhao, Coalescence of Al_{0.3}CoCrFeNi polycrystalline high-entropy alloy in hot-pressed sintering: a molecular dynamics and phase-field study, *Npj Comput. Mater.* 9 (1) (2023) 185.
- [45] Yunus Onur Yildiz, Morphological evolution of irregularly shaped Au nanoparticles during the sintering process and their mechanical performance, *Comput. Part. Mech.* 10 (6) (2023) 1659–1667.
- [46] Xu Liu, Shizhen Li, Jiajie Fan, Jing Jiang, Yang Liu, Huaiyu Ye, Guoqi Zhang, Microstructural evolution, fracture behavior and bonding mechanisms study of copper sintering on bare DBC substrate for SiC power electronics packaging, *J. Mater. Res. Technol.* 19 (2022) 1407–1421.
- [47] Leiming Du, Xiangnan Pan, Youshi Hong, New insights into microstructure refinement in crack initiation region of very-high-cycle fatigue for SLM Ti-6Al-4V via precession electron diffraction, *Materialia* 33 (2024) 102008.
- [48] Lu Qi, Suyun He, Chunjin Chen, Binbin Jiang, Yulin Hao, Hengqiang Ye, Rui Yang, Kui Du, Diffusional-displacive transformation in a metastable β titanium alloy and its strengthening effect, *Acta Mater.* 195 (2020) 151–162.
- [49] Xin Liu, Yu Zhou, Xinjie Zhu, Duoduo Wang, Qunbo Fan, The failure mechanism at adiabatic shear bands of titanium alloy: high-precision survey using precession electron diffraction and geometrically necessary dislocation density calculation, *Mater. Sci. Engineering: A* 746 (2019) 322–331.
- [50] Teng-Jan Chang, Hsing-Yang Chen, Chin-I Wang, Hsin-Chih Lin, Chen-Feng Hsu, Jer-Fu Wang, Chih-Hung Nien, Chih-Sheng Chang, Iuliana P Radu, Miin-Jang Chen, Wake-up-free ferroelectric Hf_{0.5}Zr_{0.5}O₂ thin films characterized by precession electron diffraction, *Acta Mater.* 246 (2023) 118707.
- [51] Niels Cautelaerts, Edgar F Rauch, Jiwon Jeong, Gerhard Dehm, Christian H Liebscher, Investigation of the orientation relationship between nano-sized G-phase precipitates and austenite with scanning nano-beam electron diffraction using a pixelated detector, *Scr. Mater.* 201 (2021) 113930.
- [52] Hongyu Xiao, Zhiping Wang, Jiwei Geng, Chengcheng Zhang, Yugang Li, Qing Yang, Mingliang Wang, Dong Chen, Zhuoguo Li, Haowei Wang, Precipitation and crystallographic relationships of nanosized η/η' precipitates at S-Al interface in Al-Zn-Mg-Cu alloy, *Scr. Mater.* 214 (2022) 114643.
- [53] Jiwon Jeong, Niels Cautelaerts, Gerhard Dehm, Christian H Liebscher, Automated crystal orientation mapping by precession electron diffraction-assisted four-dimensional scanning transmission electron microscopy using a scintillator-based CMOS detector, *Microsc. Microanal.* 27 (5) (2021) 1102–1112.
- [54] Mario F Heinig, Dipanwita Chatterjee, Antonius TJ van Helvoort, Jakob Birkedal Wagner, Shima Kadkhodazadeh, Håkon Wriek Ånes, Frank Niessen, Alice Bastos da Silva Fanta, High resolution crystallographic orientation mapping of ultrathin films in SEM and TEM, *Mater. Charact.* 189 (2022) 111931.
- [55] Ronan Henry, Thierry Blay, Thierry Douillard, Arnel Descamps-Mandine, Isabelle Zacharie-Aubrun, Jean-Marie Gatt, Cyril Langlois, Sylvain Meille, Local fracture toughness measurements in polycrystalline cubic zirconia using micro-cantilever bending tests, *Mech. Mater.* 136 (2019) 103086.
- [56] Daniel Sorensen, Eric Hintsala, Joseph Stevick, Jesse Fischlar, Bernard Li, Daniel Kiener, Jason C Myers, Hui Jin, Jia Liu, Douglas Stauffer, et al., Intrinsic toughness of the bulk-metallic glass Vitreloy 105 measured using micro-cantilever beams, *Acta Mater.* 183 (2020) 242–248.
- [57] Hao Zhang, Chuantong Chen, Jinting Jiu, Shijo Nagao, Katsuaki Sukanuma, Microstructural homogeneity of sintered Ag joint after pressureless sintering process, in: 2017 International Conference on Electronics Packaging, ICEP, IEEE, 2017, pp. 122–124.
- [58] Chuantong Chen, Zheng Zhang, Dongjin Kim, Tetsuya Sasamura, Yukinori Oda, Ming-Chun Hsieh, Aya Iwaki, Aiji Suetake, Katsuaki Sukanuma, Interface reaction and evolution of micron-sized Ag particles paste joining on electroless Ni-/Pd-/Au-finished DBA and DBC substrates during extreme thermal shock test, *J. Alloys Compd.* 862 (2021) 158596.
- [59] Fan Yang, Wenbo Zhu, Weizhen Wu, Hongjin Ji, Chunjin Hang, Mingyu Li, Microstructural evolution and degradation mechanism of SiC-Cu chip attachment using sintered nano-Ag paste during high-temperature ageing, *J. Alloys Compd.* 846 (2020) 156442.

- [60] Tamás Csanádi, Ahmad Azizpour, Marek Vojtko, William G Fahrenholtz, The effect of crystal anisotropy on fracture toughness and strength of ZrB₂ microcantilevers, *J. Am. Ceram. Soc.* 107 (3) (2024) 1669–1681.
- [61] Jicheng Gong, Angus J. Wilkinson, Anisotropy in the plastic flow properties of single-crystal α titanium determined from micro-cantilever beams, *Acta Mater.* 57 (19) (2009) 5693–5705.
- [62] Gerhard Dehm, Balila Nagamani Jaya, Rejin Raghavan, Christoph Kirchlechner, Overview on micro-and nanomechanical testing: New insights in interface plasticity and fracture at small length scales, *Acta Mater.* 142 (2018) 248–282.
- [63] Aidan P Thompson, H Metin Aktulga, Richard Berger, Dan S Bolintineanu, W Michael Brown, Paul S Crozier, Pieter J In't Veld, Axel Kohlmeyer, Stan G Moore, Trung Dac Nguyen, et al., LAMMPS-a flexible simulation tool for particle-based materials modeling at the atomic, meso, and continuum scales, *Comput. Phys. Comm.* 271 (2022) 108171.
- [64] Alexander Stukowski, Visualization and analysis of atomistic simulation data with OVITO—the open visualization tool, *Modelling Simul. Mater. Sci. Eng.* 18 (1) (2009) 015012.
- [65] Yu Mishin, MJ Mehl, DA Papaconstantopoulos, AF Voter, JD Kress, Structural stability and lattice defects in copper: Ab initio, tight-binding, and embedded-atom calculations, *Phys. Rev. B* 63 (22) (2001) 224106.
- [66] Yu Mishin, M. Asta, Ju Li, Atomistic modeling of interfaces and their impact on microstructure and properties, *Acta Mater.* 58 (4) (2010) 1117–1151.
- [67] Timofey Frolov, David L. Olmsted, Mark Asta, Yuri Mishin, Structural phase transformations in metallic grain boundaries, *Nat. Commun.* 4 (1) (2013) 1899.
- [68] Jian Han, Spencer L. Thomas, David J. Srolovitz, Grain-boundary kinetics: A unified approach, *Prog. Mater. Sci.* 98 (2018) 386–476.
- [69] B. Henrich, A. Wonisch, T. Kraft, M. Moseler, H. Riedel, Simulations of the influence of rearrangement during sintering, *Acta Mater.* 55 (2) (2007) 753–762.
- [70] Douglas E Spearot, Mark A Tschopp, Karl I Jacob, David L McDowell, Tensile strength of $\langle 1\ 0\ 0 \rangle$ - and $\langle 1\ 1\ 0 \rangle$ -tilt bicrystal copper interfaces, *Acta Mater.* 55 (2) (2007) 705–714.
- [71] Daniel Trias, Josep Costa, Albert Turon, J.E. Hurtado, Determination of the critical size of a statistical representative volume element (SRVE) for carbon reinforced polymers, *Acta Mater.* 54 (13) (2006) 3471–3484.
- [72] I.M. Gitman, Harm Askes, L.J. Sluys, Representative volume: Existence and size determination, *Eng. Fract. Mech.* 74 (16) (2007) 2518–2534.
- [73] Swantje Bargmann, Benjamin Klusemann, Jürgen Markmann, Jan Eike Schnabel, Konrad Schneider, Celal Soyarslan, Jana Wilmers, Generation of 3D representative volume elements for heterogeneous materials: A review, *Prog. Mater. Sci.* 96 (2018) 322–384.
- [74] Xiaohui Tu, Ahmad Shahba, Jinlei Shen, Somnath Ghosh, Microstructure and property based statistically equivalent RVEs for polycrystalline-polyphase aluminum alloys, *Int. J. Plast.* 115 (2019) 268–292.
- [75] R.B. Vieira, H. Sehitoglu, J. Lambros, Representative volume elements for plasticity and creep measured from high-resolution microscale strain fields, *Acta Mater.* 214 (2021) 117021.
- [76] Joseph Lifton, Tong Liu, An adaptive thresholding algorithm for porosity measurement of additively manufactured metal test samples via X-ray computed tomography, *Addit. Manuf.* 39 (2021) 101899.
- [77] Małgorzata Makowska, Pradeep Vallachira Warriam Sasikumar, Lorenz Hagelüken, Dario F Sanchez, Nicola Casati, Federica Marone, Gurdial Blugan, Jürgen Brugger, Helena Van Swygenhoven, Cracks, porosity and microstructure of Ti modified polymer-derived SiOC revealed by absorption-, XRD- and XRF-contrast 2D and 3D imaging, *Acta Mater.* 198 (2020) 134–144.
- [78] Hans E. Exner, Eduard Arzt, Sintering processes, *Sinter. Key Pap.* (1990) 157–184.
- [79] Wole Soboyejo, *Mechanical Properties of Engineered Materials*, CRC Press, 2002.
- [80] Xu Long, Chongyang Du, Zhen Li, Hongcun Guo, Yao Yao, Xiuzhen Lu, Xiaowu Hu, Lilei Ye, Johan Liu, Finite element analysis to the constitutive behavior of sintered silver nanoparticles under nanoindentation, *Int. J. Appl. Mech.* 10 (10) (2018) 1850110.
- [81] Yutai Su, Ziyi Shen, Xu Long, Chuantong Chen, Lehua Qi, Xujiang Chao, Gaussian filtering method of evaluating the elastic/elasto-plastic properties of sintered nanocomposites with quasi-continuous volume distribution, *Mater. Sci. Engineering: A* 872 (2023) 145001.
- [82] Yutai Su, Jiaqi Zhu, Xu Long, Liguang Zhao, Chuantong Chen, Changqing Liu, Statistical effects of pore features on mechanical properties and fracture behaviors of heterogeneous random porous materials by phase-field modeling, *Int. J. Solids Struct.* 264 (2023) 112098.
- [83] Jörg Hohe, Volker Hardenacke, Analysis of uncertainty effects due to microstructural disorder in cellular or porous materials, *Int. J. Solids Struct.* 49 (7–8) (2012) 1009–1021.
- [84] Gong He, Yao Yao, Yang Yuting, Size effect on the fracture of sintered porous nano-silver joints: Experiments and Weibull analysis, *J. Alloys Compd.* 863 (2021) 158611.